InP-based Waveguide Photodetector with Integrated Photon Multiplication

D. Pasquariello, J. Piprek, D. Lasaosa, and J. E. Bowers

Electrical and Computer Engineering Department
University of California, Santa Barbara, CA 93106

ABSTRACT

We report on novel InP-based traveling-wave amplification photodetectors exhibiting an external quantum efficiency of more than 100%. Our detectors vertically combine a bulk InGaAs photodetector ridge region with laterally confined InGaAsP quantum wells for amplification. In addition to ultra high responsivities, such detectors have the potential to also achieve high saturation power and high speed. The device physics is discussed using advanced numerical simulation.

Keywords: photodetector, waveguide, amplifier, integrated photonics, optical gain, III-V semiconductor devices, numerical simulation

1. INTRODUCTION

Desirable properties for detectors in analog fiber-optical links are high efficiency, large bandwidth and high saturation power. For these applications there is an increasing interest in waveguide photodetectors, were the efficiency-bandwidth trade-off present in surface-illuminated photodetectors is circumvented. Traveling-wave photodetectors (TWPDs) are able to simultaneously achieve large bandwidth and high responsivity. The optical power propagates perpendicular to the carrier extraction and therefore the efficiency and the carrier transit time can be tuned independently. However, the photocurrent is still limited by saturation effects at higher optical power. In order to overcome this limitation, we have recently proposed the traveling-wave amplification photodetector (TAP detector, Fig. 1)[1,2] . The TAP detector has an integrated light amplification region, which makes it possible to maintain a nearly constant optical power level along the device. The optical power is kept below the saturation limit and very high photo currents can be achieved with long devices, higher than with any other photodetector.[3] This is of great importance, for instance with fiber-optic analog links whose performance is often limited by optical loss. Signal amplification in our TAP detector enables net link gain.

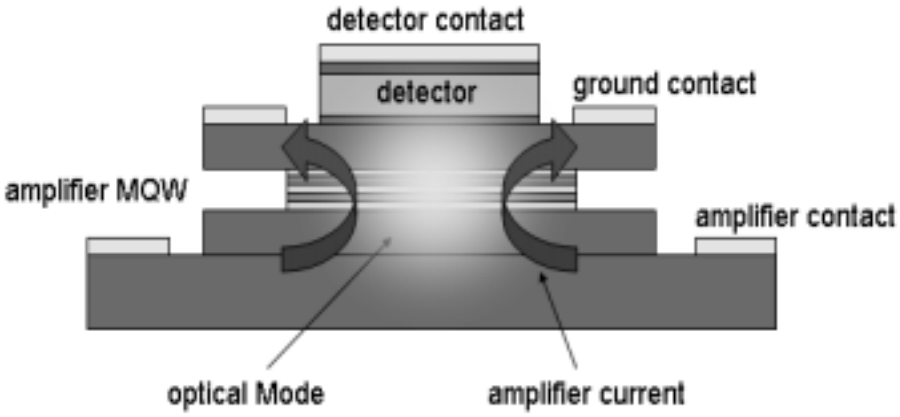

Figure 1. Cross section of our InP TAP detector.

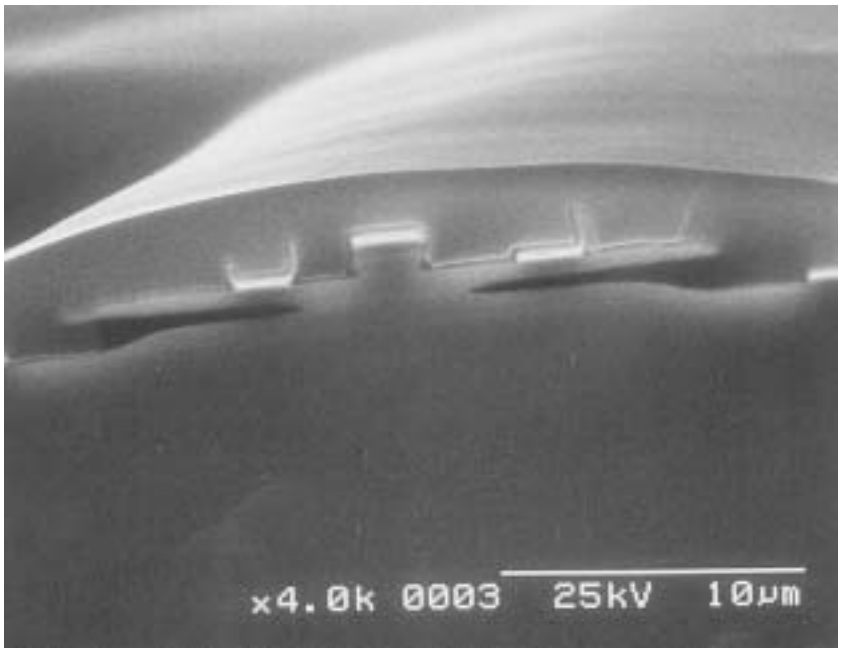

Figure 2. Facet view of the InP TAP detector.

2. DEVICE FABRICATION

A schematic cross-sectional view of the device is shown in Fig. 1. Epitaxial layers were grown in a single run by metal-organic vapour-phase epitaxy (MOVPE) on semi-insulating InP. A 250 nm thick i-InGaAs layer was used as the absorber and optical gain was obtained from six 1% compressively strained InGaAsP quantum wells. The layer structure is listed in Tab. 1. Optical and electrical confinement in the center of the device is provided by the ridge-waveguide structure as well as by lateral under etching. Previous generations of our InP TAP detector used an n-p-n structure which was found to restrict the lateral current spreading within the p-doped ground contact layer leading to low quantum well gain in the center of the device.[4] The optimized device design presented in this paper features a p-n-p structure which allows for more uniform optical gain within the quantum wells. The detector p-contact is Ti/Pt/Au, the ground n-contact consisted of Ni/AuGe/Ni/Au and a Pd/Zn/Pd/Au metallization was used for the amplifier p-contact. After cleaving, the waveguide photodetectors were anti-reflection-coated with 2200 $\mathring{A}$ SiO_x.

SEM pictures of fabricated devices are given in Figs. 2 and 3. The first figure shows a facet view, including the underetched InGaAsP multi-quantum well (MQW) amplifier layers. The second figure shows the complete device. The coplanar microwave (CPW) probe pads are visible in the background.

3. MEASUREMENTS

A lensed fiber with a spot size of 2.5 μm is used to couple light into the waveguide. The laser source is operated at 1550 nm wavelength. The measured photoresponse is plotted in Fig. 4 for a 145 μm long waveguide. The input signal power is 2.1 μW in this case. At low amplifier bias current there is not much increase in photocurrent. However, once the amplifier is biased above transparency the input signal start experiencing gain. An external quantum efficiency of 110%, corresponding to a responsivity of 1.375 A/W, was obtained for an amplifier bias current of 60 mA. At higher bias currents thermal roll-over dominates the amplifier characteristics.

The efficiency in Fig. 4 is due to pure photocurrent from the input signal. The contribution from spontaneous emission has been removed by first measuring the background current in the detector without signal. This background current is then subtracted from the total photocurrent measurement with signal. The background current includes contributions from dark current, leakage current, and detected spontaneous emission generated in the amplifier. Figure 5 shows typical amplified spontaneous emission (ASE) and detector background current behavior. The output ASE

Table 1. Epitaxial layer structure of the pnp TAP detector (l - layer thickness, N_{dop} - doping, n_{r} - refractive index at 1550 nm wavelength). Intrinsic (i) layers are assumed to exhibit low n-type background doping.

Parameter	l	N_{dop}	n_{r}
Unit	nm	1/cm^3	-
p-In$_{0.53}$Ga$_{0.47}$As (D contact)	100	1×10^{20}	3.608
p-InP (cladding)	50	1×10^{18}	3.165
p-InP (cladding)	50	1×10^{17}	3.165
i-InP (doping offset)	70	1×10^{16}	3.165
i-In$_{0.53}$Ga$_{0.47}$As (detector)	250	1×10^{16}	3.608
n-InP (cladding)	50	1×10^{17}	3.165
n-InP (cladding)	300	1×10^{18}	3.165
n-InP (cladding)	50	3×10^{18}	3.165
n-In$_{0.85}$Ga$_{0.15}$As$_{0.32}$P$_{0.68}$ (G contact)	100	3×10^{18}	3.282
n-InP (cladding)	50	3×10^{18}	3.165
n-InP (cladding)	300	1×10^{18}	3.165
n-InP (cladding)	100	1×10^{17}	3.165
i-In$_{0.82}$Ga$_{0.18}$As$_{0.4}$P$_{0.6}$ (waveguide)	100	1×10^{16}	3.311
i-In$_{0.71}$Ga$_{0.29}$As$_{0.55}$P$_{0.45}$ (barrier)	17	1×10^{16}	3.367
i-In$_{0.76}$Ga$_{0.24}$As$_{0.79}$P$_{0.21}$ (well)	6.4	1×10^{16}	3.616
i-In$_{0.71}$Ga$_{0.29}$As$_{0.55}$P$_{0.45}$ (barrier)	8	1×10^{16}	3.367
i-In$_{0.76}$Ga$_{0.24}$As$_{0.79}$P$_{0.21}$ (well)	6.4	1×10^{16}	3.616
i-In$_{0.71}$Ga$_{0.29}$As$_{0.55}$P$_{0.45}$ (barrier)	8	1×10^{16}	3.367
i-In$_{0.76}$Ga$_{0.24}$As$_{0.79}$P$_{0.21}$ (well)	6.4	1×10^{16}	3.616
i-In$_{0.71}$Ga$_{0.29}$As$_{0.55}$P$_{0.45}$ (barrier)	8	1×10^{16}	3.367
i-In$_{0.76}$Ga$_{0.24}$As$_{0.79}$P$_{0.21}$ (well)	6.4	1×10^{16}	3.616
i-In$_{0.71}$Ga$_{0.29}$As$_{0.55}$P$_{0.45}$ (barrier)	8	1×10^{16}	3.367
i-In$_{0.76}$Ga$_{0.24}$As$_{0.79}$P$_{0.21}$ (well)	6.4	1×10^{16}	3.616
i-In$_{0.71}$Ga$_{0.29}$As$_{0.55}$P$_{0.45}$ (barrier)	8	1×10^{16}	3.367
i-In$_{0.76}$Ga$_{0.24}$As$_{0.79}$P$_{0.21}$ (well)	6.4	1×10^{16}	3.616
i-In$_{0.71}$Ga$_{0.29}$As$_{0.55}$P$_{0.45}$ (barrier)	17	1×10^{16}	3.367
i-In$_{0.82}$Ga$_{0.18}$As$_{0.4}$P$_{0.6}$ (waveguide)	100	1×10^{16}	3.311
i-InP (doping offset)	500	1×10^{16}	3.165
p-InP (cladding)	100	1×10^{18}	3.165
p-In$_{0.72}$Ga$_{0.28}$As$_{0.6}$P$_{0.4}$ (A contact)	100	4×10^{18}	3.396
p-InP (cladding)	100	1×10^{18}	3.165
i-InP (buffer)	500	1×10^{16}	3.165

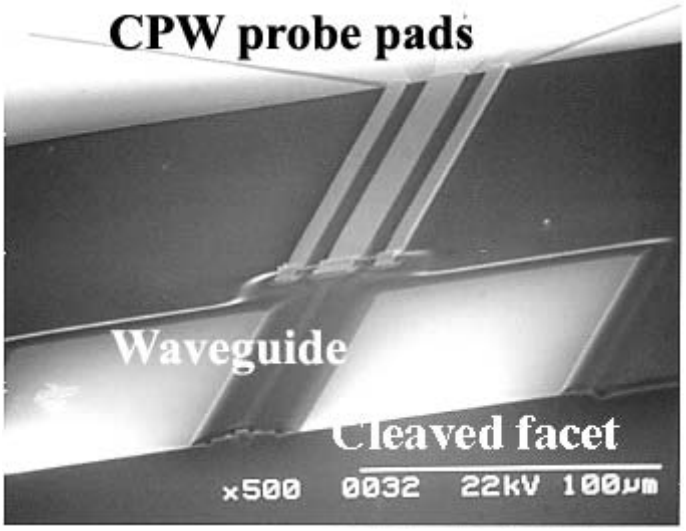

Figure 3. Top view of the final device incl. coplanar microwave pads.

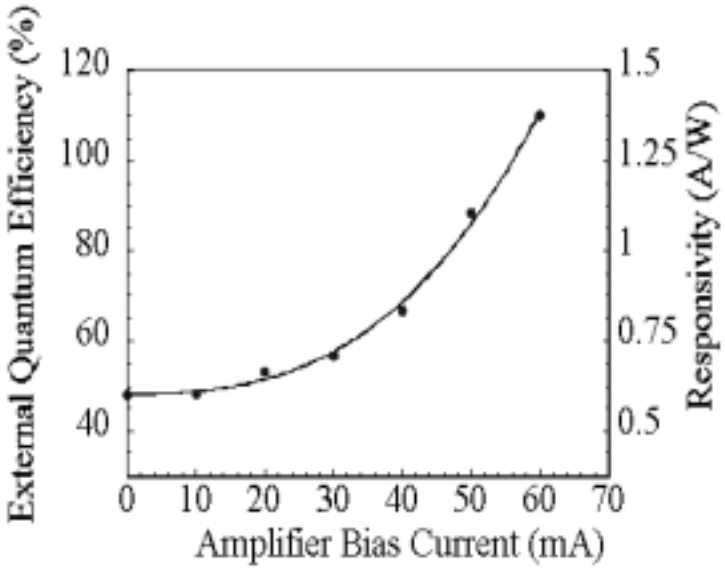

Figure 4. Measured detector response vs. amplifier current.

was measured at the cleaved facet using an external broad area detector. It is clearly seen that the dominating background current contribution in the detector comes from ASE in the amplifier. The background current in the detector follows the output ASE almost exactly and rolls over at the same point. Competition between ASE and signal for the available gain is expected to result in a measured efficiency that is lower than the actual efficiency.[5]

4. SIMULATION AND ANALYSIS

In order to analyze the performance of our device, we utilize advanced device simulation software.[6,7] The underlying theoretical models are discussed elsewhere.[8]

Figure 6 shows the band diagram at the vertical axis of the device. The common band offset ratio of $\Delta E_c/\Delta E_v = 40:60$ is employed at all interfaces. The conduction bands of the active layers are assumed parabolic and the non-parabolic valence bands are calculated by the two-band $\vec{k}\cdot\vec{\mathbf{p}}$ method. The free carrier model for stimulated band-to-band transitions is employed to compute both gain and absorption for the amplification layers and the detection layer, respectively. The calculated spectra are plotted in Fig. 7 for different carrier densities. At low carrier density (reverse bias),

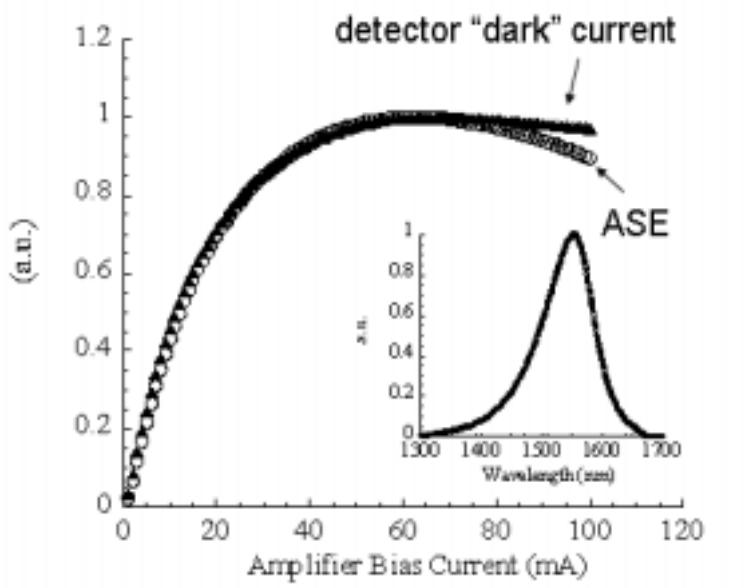

Figure 5. Amplified spontaneous emission (ASE) and background ("dark") current vs. amplifier current (no input signal). The inset shows the ASE spectrum.

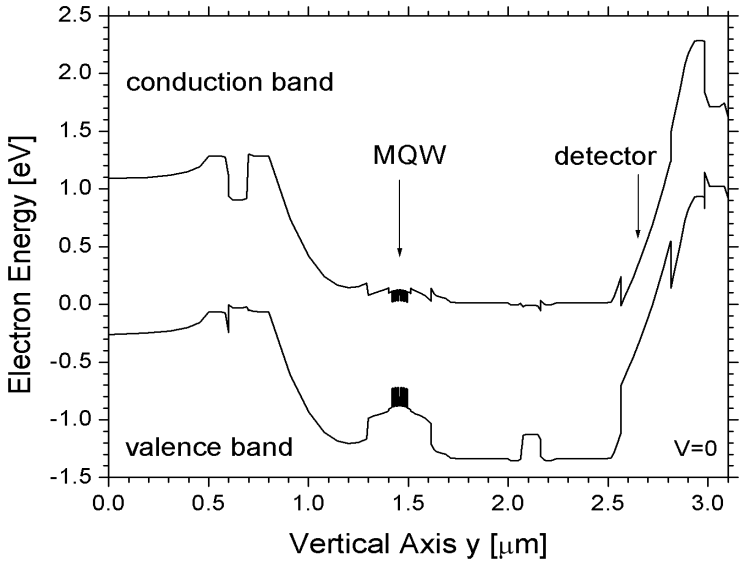

Figure 6. Vertical energy band diagram at zero bias.

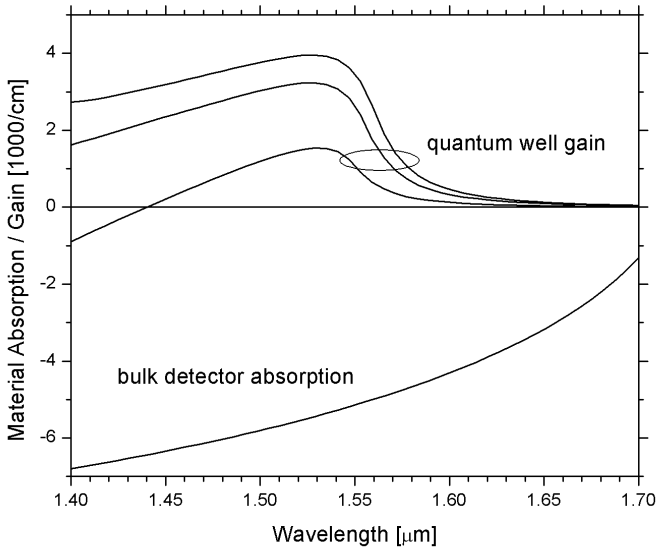

Figure 7. Gain and absorption spectra for quantum well and detector, respectively. Gain spectra are calculated at three carrier densities: 2, 4, and $6\times10^{18}\mathrm{cm}^{-3}$, the absorption is calculated at $10^{16}\mathrm{cm}^{-3}$.

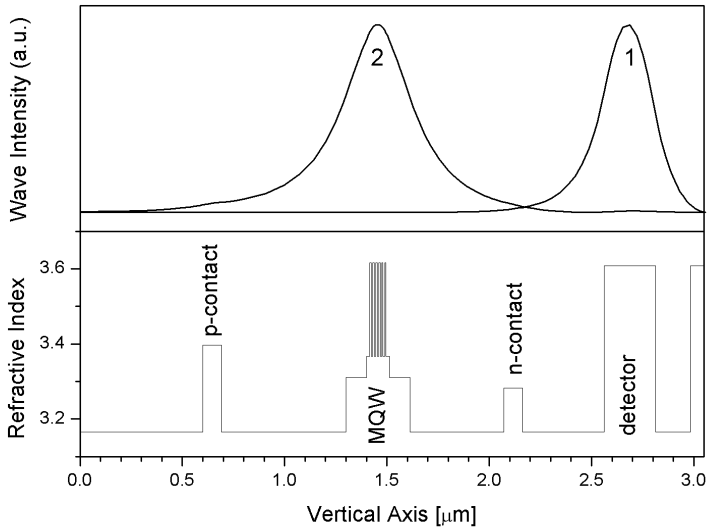

Figure 8. Vertical profile for two vertical waveguide modes (top) and for the refractive index at 1550 nm wavelength (bottom).

the bulk InGaAs detector layer exhibits an absorption coefficient of about 5000 cm^{-1} at 1550 nm wavelength which is reasonably close to measured values near 6000 cm^{-1}. With forward bias, the carrier density in the quantum well amplification layers is much higher. At 1550 nm wavelength, the gain reaches about 2500 cm^{-1} for a carrier density of $4\times10^{18}\mathrm{cm}^{-3}$. However, the total amplification layer thickness of 42 nm is much smaller than the absorption layer thickness of 250 nm. Thus, optical waveguide modes are preferred that exhibit little overlap with the detector region.

The vertical index profile of our device is plotted in Fig. 8 together with the two main waveguide modes. Mode 1 is mainly located in the detector region and mode 2 in the amplifier region. The two-dimensional profile of the amplifier mode 2 is shown in Fig. 9 for 2 micron ridge width and 6 micron

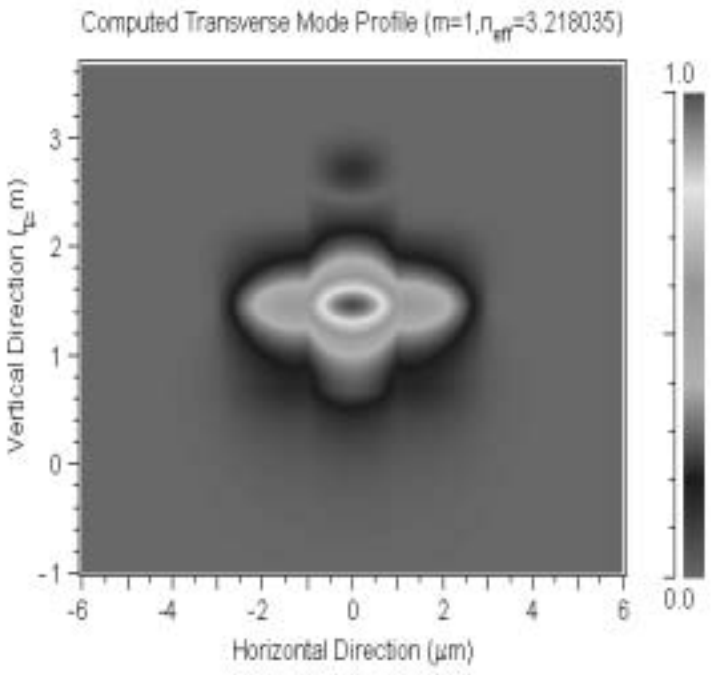

Figure 9. Two-dimensional intensity profile of the amplifier mode.

Mode	Γ_{amp}	Γ_{det}	c_{f}
1	0.0025	0.6177	0.11
2	0.0689	0.0032	0.57

Table 2. Fiber coupling factor c_{f} and optical confinement factors Γ_{amp} and Γ_{det} of vertical modes for the amplifier and the detector region, respectively.

MQW aperture (cf. Figs. 2). Considering a perfect alignment of the optical fiber, th ecoupling factor from the fiber mode to this amplifier mode is as high as 0.57 while the detector mode receives only about 11% of the signal power. The coupling factors as well as the optical confinement factors Γ_{amp} and Γ_{det} are given in Tab. 2. The total modal gain of each mode can be estimated as

$$g_{\mathsf{mode}} = \Gamma_{\mathsf{amp}} g_{\mathsf{amp}} - \Gamma_{\mathsf{det}} \alpha_{\mathsf{det}} \tag{1}$$

with g_{amp} and α_{det} from Fig. 7. The detector mode 1 quickly decays along the waveguide, since there is no overlap with the amplifier region. Additional photons generated by stimulated recombination in the quantum wells stay within the same optical mode as the incoming photon. A balance between photon generation and absorption can only be achieved by mode 2. Relatively low pumping is sufficient to increase the optical power of mode 2 as it travels down the waveguide. Figure 10 gives the MQW modal gain of the amplifier mode 2 as function of the amplifier current. Quantum well transparency is achieved at about 10 mA current. Considering the measured InGaAs absorption coefficient of 6300 cm^{-1} at 1550 nm wavelength, the MQW gain of mode 2 compensates for the detector loss at 20 mA amplifier current. Net amplification dominates for currents above 20 mA. These theoretical results are in excellent agreement with the experimental results in Fig. 4.

5. CONCLUSION

We demonstrate more than 100% external quantum efficiency with an InP-based traveling-wave amplification photodetector. The device physics is analyzed using advanced numerical simulation. Good agreement with the measurement is obtained and the prefered optical waveguide mode is identified. The theoretical model shall be used for further device optimization. In order to increase

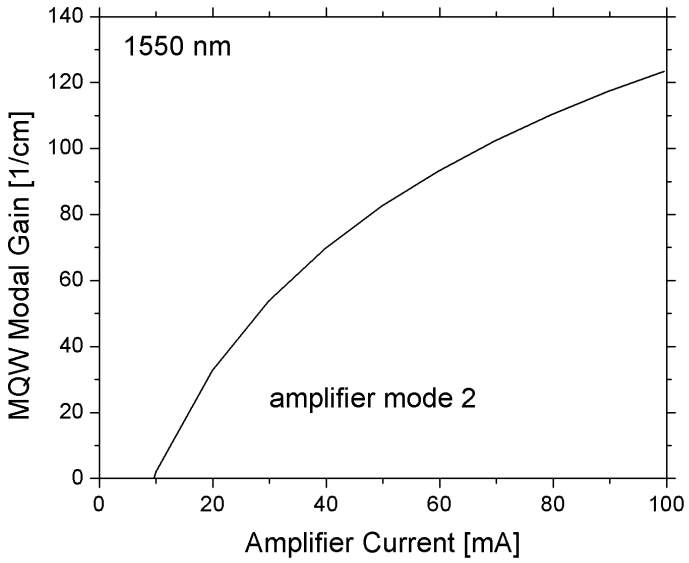

Figure 10. Amplifier gain for mode 2 calculated as function of amplifier current.

the MQW photon generation as well as the detector absorption, for example, both the optical confinement factors of the amplifier mode should be increased in a balanced way.

REFERENCES

1. D. Lasaosa, Y. J. Chiu, J. Piprek, and J. E. Bowers, "Traveling-wave amplification photodetector (TAP detector)," in 13th Lasers and Electro-Optics Society Annual Meeting, (Piscataway), pp. 260–261, Institute of Electrical and Electronic Engineers, 2000.
2. D. Lasaosa, Y. J. Chiu, J. Piprek, and J. E. Bowers, "Modeling of traveling-wave amplification photodetectors," in Physics and Simulation of Optoelectronic Devices IX, Proc. SPIE 4283-64, 2001.
3. J. Piprek, D. Lasaosa, D. Pasquariello, and J. E. Bowers, "Optimization of GaAs Amplification Photodetectors for 700% Quantum Efficiency," IEEE J. Sel. Top. Quant. Electr., vol. 9, 2003 (to be published).
4. J. Piprek, D. Pasquariello, D. Lasaosa, and J. E. Bowers, "Novel Waveguide Photodetectors on InP with Integrated Light Amplification," in Compound Semiconductors, Proc. ECS 2003-04, pp. 1-8, 2003.
5. D. Lasaosa, D. Pasquariello, J. Piprek, and J. E. Bowers, "Recent Advances in Photodetectors with Distributed Light Amplification," in Active and Passive Optical Components for WDM Commuinications III, Proc. SPIE 5246-172, 2003.
6. APSYS by Crosslight Software, 2002.
7. BeamProp by RSoft Design Group, 2002.
8. J. Piprek, Semiconductor Optoelectronic Devices - Introduction to Physics and Simulation. San Diego: Academic Press, 2003.